Medium Spatial Resolution Satellite Imagery for Estimating and Mapping Urban Impervious Surfaces Using LSMA and ANN

Qihao Weng, *Member, IEEE*, and Xuefei Hu

Abstract—Remote sensing estimation of impervious surface is significant in monitoring urban development and determining the overall environmental health of a watershed, and it has therefore attracted more interest recently in the remote sensing community. The main objective of this paper is to examine and compare the effectiveness of two advanced algorithms for estimating impervious surfaces from medium spatial resolution satellite images, namely, linear spectral mixture analysis (LSMA) and artificial neural network (ANN). Terra's Advanced Spaceborne Thermal Emission and Reflection Radiometer [(ASTER); acquired on June 16, 2001] and a Landsat Enhanced Thematic Mapper Plus (ETM+) image (acquired on June 22, 2000) of Indianapolis, IN, were used for the analysis. The LSMA was employed to generate high- and low-albedo, vegetation, and soil fraction images (endmembers), and an image of impervious surfaces was then estimated by adding high- and low-albedo fraction images. Furthermore, an ANN model, specifically the multilayer-perceptron feedforward network with the back-propagation learning algorithm, was employed as a subpixel image classifier to estimate impervious surfaces. Accuracy assessment was performed against a high-resolution digital orthophoto. The results show that ANN was more effective than LSMA in generating impervious surfaces with high statistical accuracy. For the ASTER image, the root-mean-square error (RMSE) of the impervious surface map with the ANN model was 12.3%, and the one that resulted from LSMA was 13.2%. For the ETM+ image, the RMSE with the ANN model was 16.7%, and the one from LSMA was 18.9%. The better performance of ANN over LSMA is mainly attributable to the ANN's capability of handling the nonlinear mixing of image spectrum. In order to test the seasonal sensitivity of satellite images for estimating impervious surfaces, LSMA was applied to two additional ASTER images of the same area, which are acquired on April 5, 2004, and October 3, 2000, respectively. The results were then compared with the ASTER image acquired in June in terms of RMSE. The June image had the highest accuracy, whereas the October image was better than the one in April. Plant phenology caused changes in the variance partitioning and impacted the mixing-space characterization, leading to a less accurate estimation of impervious surfaces.

Index Terms—Artificial neural network (ANN), impervious surface estimation, linear spectral mixture analysis (LSMA), medium-resolution satellite images.

I. INTRODUCTION

IMPERVIOUS surfaces are anthropogenic features through which water cannot infiltrate into the soil, such as roads, driveways, sidewalks, parking lots, rooftops, and so on, and they are made of materials such as concrete, asphalt, plastics, stone, brick, metal, etc. In recent years, impervious surface has emerged not only as an indicator of the degree of urbanization but also a major indicator of environmental quality [1]. Therefore, estimating and mapping impervious surfaces are valuable not only for environmental management, e.g., water quality assessment, and storm water taxation, but also for urban planning, e.g., building infrastructure, and sustainable urban growth.

Estimation and mapping impervious surfaces from remotely sensed images are challenging tasks due to the complex landscape types in urban areas and the limitation in the spatial and spectral resolutions of remote sensing images. Moreover, some land cover types have similar reflectance signatures with impervious surfaces. For instance, dry soil and bright impervious surfaces may be similar in spectral response, whereas the reflectance characteristics of water, shades, and dark impervious surfaces are alike. As a result, these materials are easy to be confused with impervious surfaces. Separating impervious surfaces from nonimpervious surfaces is necessary but hard to achieve. Many methods have been developed to estimate and map impervious surfaces. For example, impervious surface information can be measured directly from aerial photos by digitizing the boundaries of impervious surface areas, by overlaying a grid with aerial photographs and further counting the number of intersections, by image classification, or by calculating the percentage of urbanization in an urban area [2]. Recently, more and more digital remote sensing methods have been developed, such as per-pixel classification, subpixel classification, decision tree, and linear regression.

Most previous research works for extraction of impervious surfaces in urban areas are by the use of medium spatial resolution (10–100 m) images, such as Landsat Thematic Mapper (TM)/Enhanced TM Plus (ETM+) [3]–[5], Terra's Advanced Spaceborne Thermal Emission and Reflection Radiometer (ASTER) [6], and EO-1 Advanced Land Imager (ALI) and Hyperion images [7]. However, both spatial and spectral resolutions are regarded as too coarse for use in urban environments because of the heterogeneity and complexity of urban impervious surface materials. The mixed-pixel problem in the urban landscapes has been recognized as a major problem,

affecting the use of remotely sensed data in thematic information extraction [8], [9]. Previous research has demonstrated the effectiveness of linear spectral mixture analysis (LSMA) in handling mixed pixels [3], [5]. However, the LSMA-based methods have a common problem, i.e., the impervious surface tends to be overestimated in the areas with small amount of impervious surface, but it is underestimated in the areas with large amount of impervious surface [5]. This problem is complicated by the assumption of LSMA, in which the spectral reflectance of a pixel is regarded as the linear combination of the spectral reflectance of the land cover types within the pixel. However, in reality, there are a lot of examples of nonlinear spectral mixing [10], [11]. The other problem with LSMA is the difficulty in endmember selection, which is caused by the within-class spectral variability [12]. A single material class (e.g., impervious surface) may be represented in several different locations in the feature space [13]. Urban areas may have substantially distinct types and amount of impervious surfaces. As a result, the traditional way of selecting image endmembers from the vertices of the triangle in the feature space may be problematic.

Artificial neural networks (ANN) have been used in remote sensing for many aspects. The most common application is for image classification [13]. Whereas the majority of previous research works have employed ANN as a per-pixel classifier [14]–[17], ANN has also been applied to estimate subpixel impervious surfaces from satellite images [18]–[20]. Furthermore, various algorithms of nonlinear models for subpixel classification have been compared [21], which indicate that multilayer perceptron (MLP) with back-propagation (BP) algorithm yielded the best result. The advantages of an ANN model include its capability of solving nonlinear relationships and no underlying assumption about the data [13]. Moreover, ANN requires fewer training samples [22]. Given these strengths of ANN, a comparison is justified between LSMA and ANN for estimating subpixel impervious surfaces. The main objective of this paper is to employ LSMA and ANN to estimate impervious surfaces from medium spatial resolution images (i.e., ASTER and Landsat ETM+ images) and compare the results in terms of statistical accuracy. Three research questions will be addressed: 1) Which technique, LSMA or ANN (in particular, MLP feedforward network), is relatively more effective for subpixel impervious surface estimation? 2) How do satellite images of different sensors affect the impervious surface estimation? 3) How do images acquired in different seasons impact the estimation of impervious surfaces?

II. STUDY AREA AND DATA SETS

Indianapolis/Marion County, IN, was chosen as the study area. The city is located on a flat plain and is relatively symmetrical, having possibilities of expansion in all directions. Similar to many other American cities, Indianapolis is rapidly increasing in population and area. The areal expansion occurs through the encroachment into the adjacent agricultural and nonurban land. Certain decision-making forces, such as density of population, distance to work, property value, and income structure, encourage some sectors of metropolitan Indianapolis

to expand faster than others. Extracting information of impervious surface from satellite images allows one to monitor urban changes over time and integrate imperviousness data with other spatial and nonspatial data for environmental management and urban planning activities.

Terra's ASTER and a Landsat ETM+ images of Marion County, IN, both of which were acquired in June, were used in this paper for comparison in order to minimize the difference in vegetation phenology. The ASTER image (June 16, 2001) had 14 bands with different spatial resolutions, two visible bands, and one near infrared (NIR) band with the spatial resolution of 15 m, six short wavelength IR (SWIR) bands with 30-m resolution, and five thermal IR (TIR) bands with the resolution of 90 m, but only the visible and near IR (VNIR) and SWIR bands were used in this paper. The ETM+ image (June 22, 2000) had one panchromatic band with 15-m spatial resolution, six reflective bands with 30-m resolution, and one TIR band with 60-m spatial resolution, but only the reflective bands were employed in this paper. A geometric correction with the nearest-neighbor resampling algorithm was conducted on both images. The root-mean-square error (RMSE) of less than 0.5 pixel was obtained from each geocorrection. The images were rectified to a Universal Transverse Mercator (UTM) coordinate system, with the pixel size of 30 m for both the ASTER and ETM+ images. A digital aerial photograph of Marion County (acquired in 2003) with a spatial resolution of 2 ft (0.61 m) was used for accuracy assessment. All the images and the aerial photo were resampled to the same projection (i.e., UTM, Zone 16, and Datum World Geodetic System 84).

III. METHODOLOGY

A. LSMA Approach

1) Concept of LSMA: LSMA is a physically based image processing method. It assumes that the spectrum measured by a sensor is a linear combination of the spectra of all components within the pixel [23], [24]. The mathematical model of LSMA can be expressed as

$$R_i = \sum_{k=1}^{n} f_k R_{ik} + \mathrm{ER}_i \qquad (1)$$

where $i = 1, \ldots, m$ (number of spectral bands), $k = 1, \ldots, n$ (number of endmembers), R_i is the spectral reflectance of band i of a pixel which contains one or more endmembers, f_k is the proportion of endmember k within the pixel, R_{ik} is the known spectral reflectance of endmember k within the pixel of band i, and ER_i is the error for band i. To solve f_k, the following conditions must be satisfied: 1) Selected endmembers should be independent of each other; 2) the number of endmembers should be less than or equal to the spectral bands used; and 3) selected spectral bands should not be highly correlated.

The estimation of endmember fraction images with LSMA involves image processing, endmember selection, unmixing solution, and the evaluation of fraction images. Of these steps, selecting suitable endmembers is the most critical one in the development of high-quality fraction images. Many methods

have been developed to select endmembers. The image-based method is more commonly used due to its ease of use and the spectra of the endmembers derived at the same scale as the original image. Because of the large dimension of original data sets and the high correlations among the spectral bands, a minimum noise fraction (MNF) transformation was applied to the Landsat and ASTER images. The MNF transformation may be considered as cascaded principal component (PC) transformation with the following steps: 1) a PC transformation; 2) the noise covariance conversion; and 3) a second PC transformation [25]. Instead of ordering the components according to the variance for a PC analysis transformation, the MNF transformation orders the components in terms of the signal-to-noise ratios [26]. As a result, most information is contained in the first few components. In this paper, the first three MNF components were used to select endmembers due to the fact that most information of the original images was contained in these components. Fig. 1 shows the MNF components extracted from ASTER and ETM+ images.

2) Endmember Selection and Spectral Unmixing: Endmembers were initially identified from the ETM+ and ASTER images based on high-resolution aerial photographs. Four types of endmembers were selected: green vegetation (vegetation), soils (including dry and dark soils), low albedo (asphalt, water, etc.), and high-albedo surfaces (concrete, sand, etc.). The vegetation was selected from the areas of dense grass and pasture. The different types of impervious surfaces were selected from building roofs, airport runway, highway intersections, etc. The soils were selected from the bare grounds in agricultural lands. Next, these initial endmembers were compared with those endmembers selected from the image scatter plots. The endmembers with similar PC spectra located at the extreme vertices of the scatter plots were finally selected. To find the best quality fraction images for the estimation of impervious surfaces, the different combinations of endmembers were examined and compared.

The visualization of fraction images, the analysis of fractional spectral properties of representative land cover types, and the assessment of error images were conducted to determine which combination provided the best fractions for each image. Because this paper was interested in estimating impervious surfaces in urban areas, the criteria for selecting suitable fraction images were as follows: 1) high-quality fraction images for the urban landscape; 2) low error; and 3) the distinction among typical land-use and land cover types in the study area.

A constrained least-squares solution was applied to unmix the six Landsat ETM+ reflective bands and nine ASTER, VNIR, and SWIR bands into fraction images. Fig. 2 shows the fraction images from the ASTER and ETM+ images. The high-albedo fractions were mainly associated with the objects with very high reflectance values, such as bright building roofs or construction materials. The low-albedo fractions mainly corresponded to the objects with very low reflectance, such as water, canopy shadow, tall-building shadows, or dark impervious surface materials. It is assumed that, in the central business district (CBD), low-albedo fraction image can be considered directly as impervious surface. For the residential and suburban areas, water and shade information contained in the low-albedo
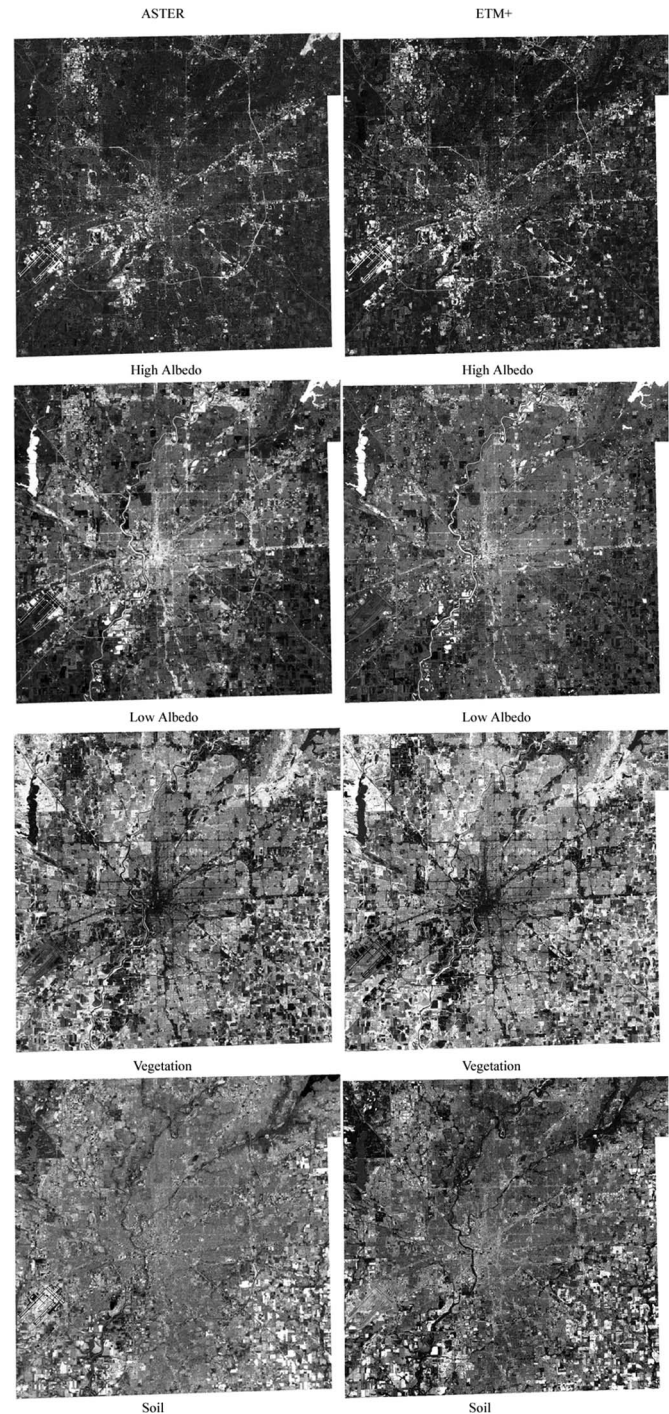

Fig. 1. MNF component images extracted from ASTER and ETM+ images.

fractions needs to be removed in the process of impervious surface estimation.

3) Impervious Surface Estimation and Refinement: Impervious surface was estimated by basing on the relationship between the reflectance of two endmembers (high and low albedos) and the reflectance of the impervious areas. By examining the relationships between impervious surfaces and the four endmembers, Wu and Murray found that the impervious surfaces were located on or near the line connecting the low- and high-albedo endmembers in the feature space [3]. An estimation procedure was thus developed by basing on

ASTER   ETM+

High Albedo   High Albedo

Low Albedo   Low Albedo
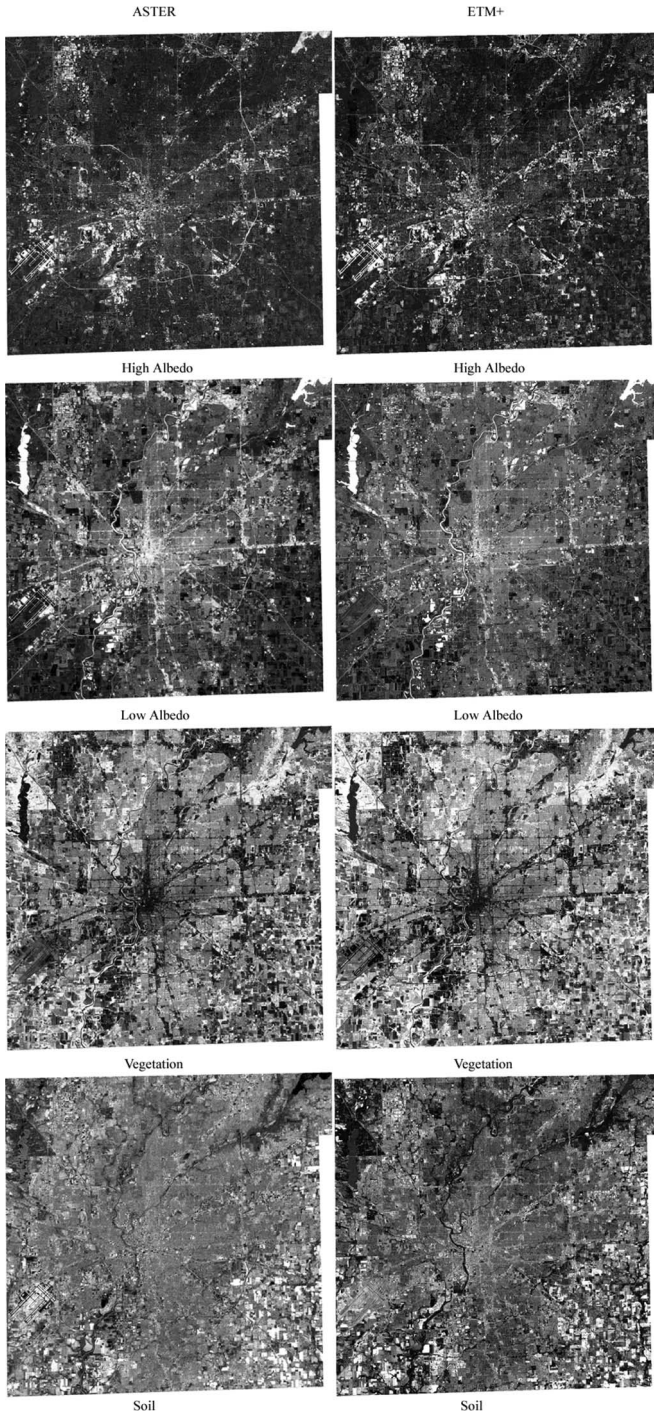
Vegetation   Vegetation

Soil   Soil

Fig. 2. Fraction images of high and low albedos, vegetation, and soil.

this relationship by adding the fractions of high- and low-albedo endmembers. The impervious surface image can be computed as

$$R_{\text{imp},b} = f_{\text{low}} R_{\text{low},b} + f_{\text{high}} R_{\text{high},b} + e_b \qquad (2)$$

where $R_{\text{imp},b}$ denotes the reflectance spectra of impervious surfaces for band b, f_{low} and f_{high} are the fractions of low and high albedos, respectively, $R_{\text{low},b}$ and $R_{\text{high},b}$ are the reflectance spectra of low and high albedos for band b, and e_b is the unmodeled residual. The fitness of this two-endmember linear spectral mixture model has been demonstrated by Wu and Murray for the CBD of Columbus, OH. This model was tested in the central part of our study area, which is the CBD of Indianapolis, and found an excellent fit with a mean RMSE value of less than 0.02 for all images.

Nevertheless, other materials existed in the high- and low-albedo fraction images, such as dry soils, water, shades, etc. These materials had similar reflectance characteristics with impervious surfaces, and they must be removed. Otherwise, the accuracy of estimation would be greatly impacted. Therefore, a refinement protocol using image masks was applied to minimize the impacts from low-reflectance (mainly water and shade) and high-reflectance materials (mainly dry soils and sand). Green vegetation and soil endmembers were considered not to contribute to the amount of impervious surface. After removing these pixels, pure impervious surfaces were estimated with the addition of low- and high-albedo endmembers by a fully constrained linear mixture model. Figs. 3 and 4 show the impervious surface images generated from ASTER and ETM+ images, respectively.

B. ANN Approach

1) Concept of MLP Feedforward Network: The MLP feed-forward network is one of the most widely used ANN models [27]. The MLP network is structured with three types of layers: input, hidden, and output layers. Each layer contains one or more nodes, which are interconnected to each other. In remote sensing digital-image applications, an MLP is usually comprised of one input layer, one or two hidden layers, and one output layer. Whereas the input-layer nodes correspond to image bands, the output-layer nodes represent the desired land use, land cover, or surface material classes. Various image processing algorithms and procedures are contained in the hidden layer. The learning algorithm is a key to the success of an ANN model. The BP learning algorithm, which is also known as the generalized delta rule, is a popular approach. During the BP training process, initial weights are initialized and assigned to each node, while training samples are inputted into the model. The results are generated and then compared to testing samples. If the accuracy level is higher than the initialized threshold value, the weights would be modified to minimize the difference between the actual and desired outputs. The process would be repeated until the predefined accuracy level is achieved.

The design of a successful ANN model is not straightforward because the effectiveness of a model is impacted by many factors, including the number of hidden layers, the hidden-layer nodes, the learning rate, the momentum factor, etc. The learning rate determines the size of the step to find the global minimum. The momentum factor helps one to find the global minimum. The estimation of these parameters may take some trial and error. In addition, a suitable number of training sites must be appropriately selected. In this paper, an MLP network with the BP learning algorithm was applied to estimate the percentage of impervious surfaces within each pixel. The ANN classifier
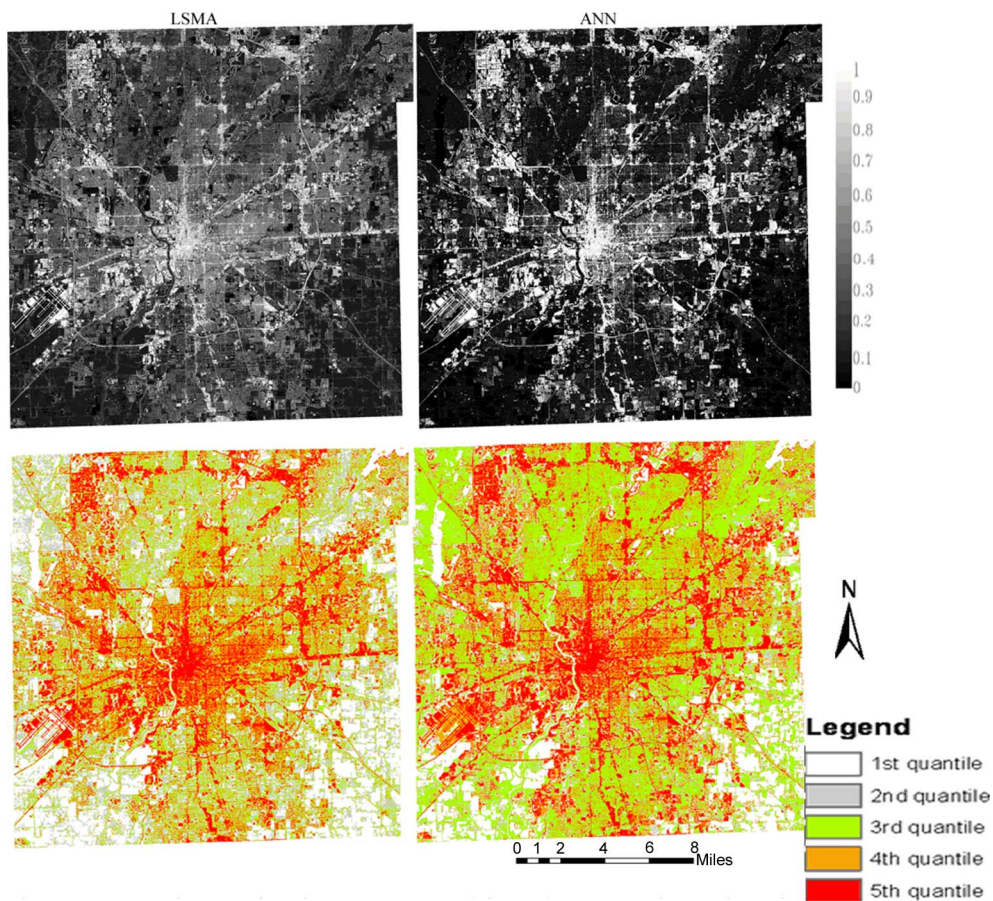
Fig. 3. Impervious surface images generated from the ASTER image by using LSMA and ANN.
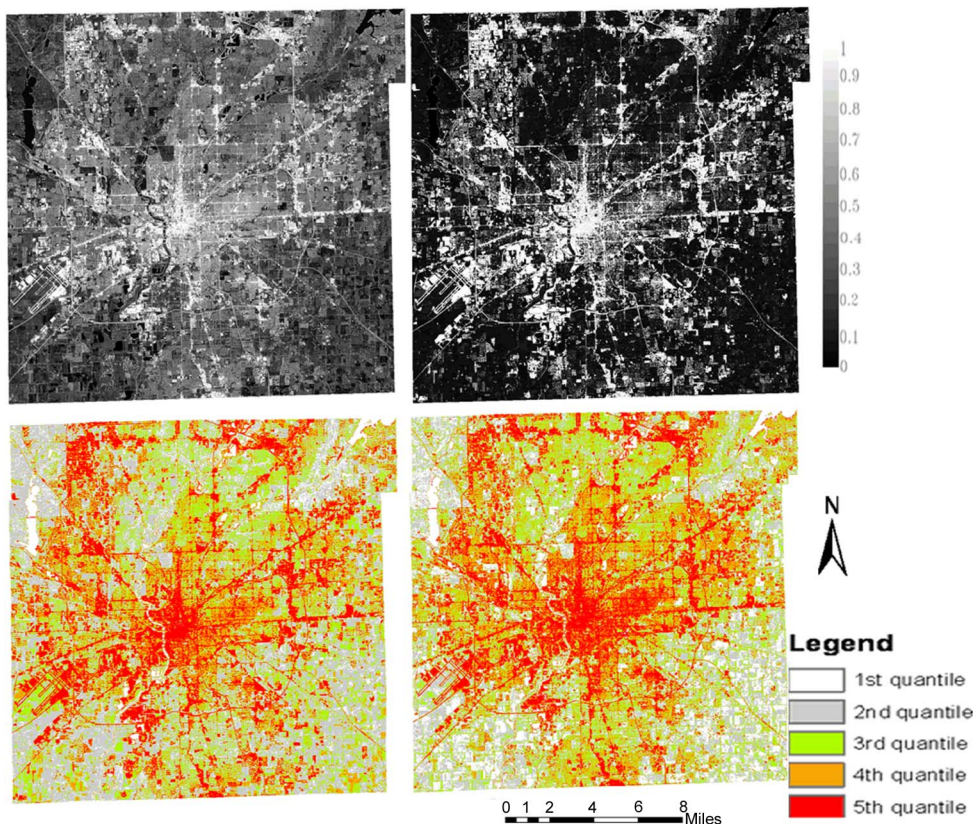

Fig. 4. Impervious surface images generated from the Landsat ETM+ image by using LSMA and ANN.
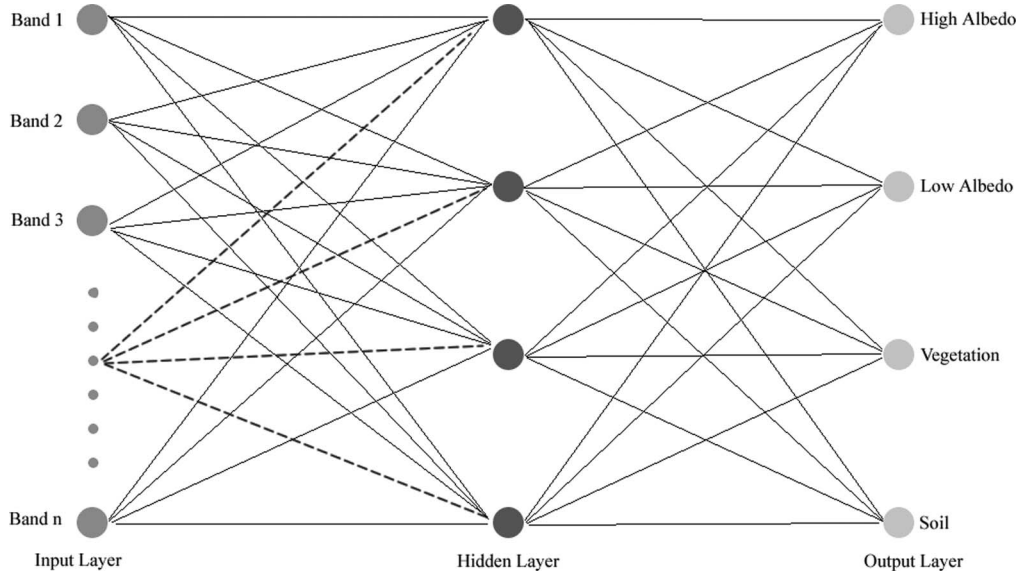
Fig. 5.   Illustration of the three-layer neural-network structure used in this paper.

used the following algorithm to calculate the input that a single node j received:

$$\text{net}_j = \sum_i w_{ij} I_i \tag{3}$$

where net_j refers to the input that a single node j receives, w_{ij} denotes the weights between nodes i and j, and I_i is the output from node i of a sender layer (input or hidden layer). The output from a node j was calculated as

$$O_j = f(\text{net}_j). \tag{4}$$

The function f is usually a nonlinear sigmoidal function known as activation function.

2) Neural Network Structure: For the ASTER image, in the input layer, nine nodes represented nine reflective bands of the ASTER image. For the ETM+ image, in the input layer, six nodes were used to represent six reflective bands of the ETM+ image. The number of nodes of the output layer was determined by the number of land cover classes. In this paper, four training surface material classes were selected, i.e., high and low albedos, vegetation, and soil. The number of hidden layer and nodes represents the complexity and power of an ANN model [27]. In general, one hidden layer is sufficient for most image classifications [28]. The number of nodes in the hidden layer could be estimated as follows [29]:

$$N_h = \text{INT}\sqrt{N_i \times N_o} \tag{5}$$

where N_h, N_i, and N_o are the number of nodes of the hidden, input, and output layers, respectively. In this paper, only one hidden layer was used, and the number of hidden-layer nodes was four in both cases. In addition, several parameters were crucial in the ANN model, such as learning rate, sigmoid function constant, momentum factor, etc. The various values of these parameters were tested in order to achieve the highest accuracy. Fig. 5 shows the neural network structure used in this paper.

In a soft classification conducted in this paper, the final results were activation-level maps. The activation-level maps were groups of images in which the value of each pixel expresses the degree that the pixel belongs to a certain class. The pixel values were between zero and one. However, the sum of the values of a certain pixel from all the land cover classes was not necessarily equal to one, because the outputs were obtained by fuzzying the signals into values in the range of zero to one with the activation function. Four activation-level maps, corresponding to high and low albedos, vegetation, and soil fractions, were eventually generated for the ASTER and ETM+ images, respectively.

3) Training and Testing Samples: The number of training samples has a significant impact on the effectiveness of the ANN model. Too few samples are not sufficient, whereas too large samples could lead to an overfit. However, larger samples were usually better than smaller samples [27]. Moreover, the characteristics and the distribution of samples were also significant. The samples should contain all the possible different spectral signatures within each class.

In this paper, 30 fields were selected for each surface cover class (i.e., high and low albedos, vegetation, and soil) from the original images. The samples were evenly distributed in each image. From all samples, 100 pixels were randomly selected for each class to be used as training pixels. Meanwhile, another 100 pixels were chosen as testing pixels. Both iteration and accuracy rate were used. The accuracy rate was set to 95% because a better result can be produced with less iterations at the accuracy level. When 95% accuracy rate cannot be reached, a predefined iteration (10 000 times in this case) would stop the training process.

C. Accuracy Assessment of Impervious Surface Maps

The accuracy assessment of impervious surface images was regarded as an important aspect of our method. Selecting a sufficient number of reference data through a proper sampling
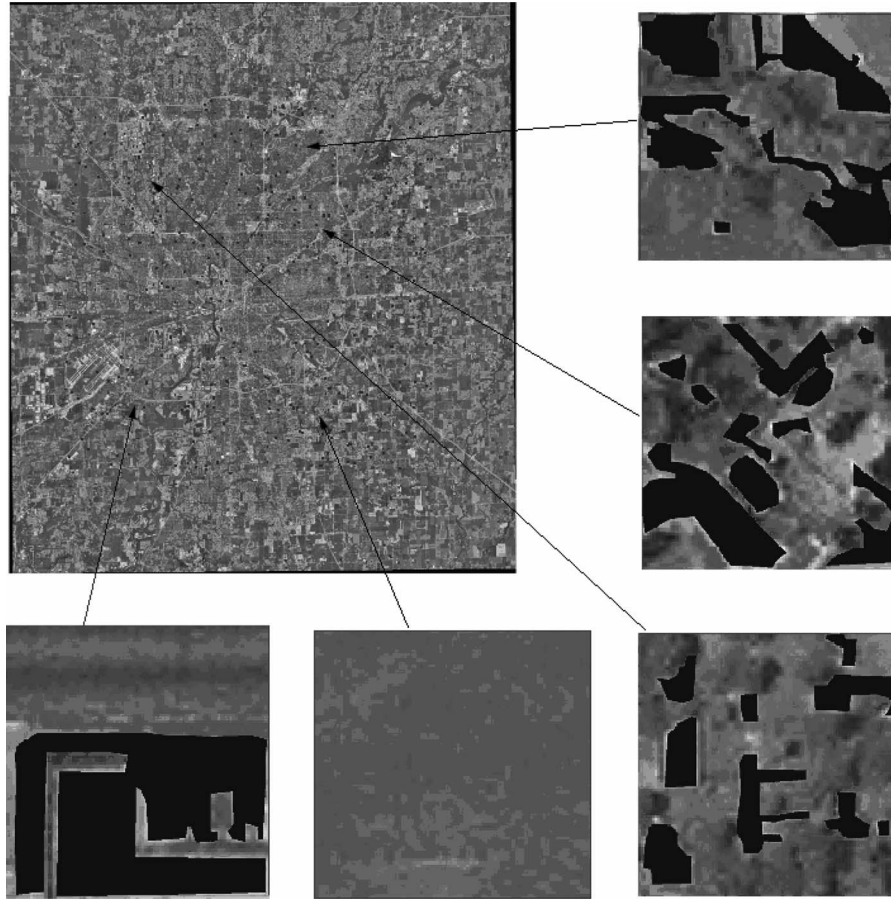
Fig. 6. Illustration of the design of sample plots and the method for obtaining reference data by digitizing impervious polygons within selected samples.

method is crucial. A total of 400 samples were selected by using a stratified random-sampling scheme. The size of each sample had a ground dimension of 90 by 90 m. For each sample, impervious surface was digitized on the corresponding Digital Ortho Quarter Quadrangles using ArcGIS. After the digitization, the proportion of impervious surface area was computed by dividing the area of impervious surface by the sampling area. Fig. 6 shows the design of sample plots and the method for obtaining reference data by digitizing impervious surface polygons within selected samples. The RMSE and the correlation coefficient (R^2) were then calculated to indicate the accuracy of the impervious surface estimation, which are expressed as follows:

$$\text{RMSE} = \sqrt{\frac{\sum\limits_{i=1}^{N}(\hat{I}_i - I_i)^2}{N}} \qquad (6)$$

$$R^2 = \frac{\sum\limits_{i=1}^{N}(\hat{I}_i - \bar{I})}{\sum\limits_{i=1}^{N}(I_i - \bar{I})^2} \qquad (7)$$

where $\hat{I}_i$ is the estimated impervious surface fraction for sample i, I_i is the impervious surface proportion computed from the aerial photo, $\bar{I}$ is the mean value of the samples, and N is the number of samples.

IV. RESULTS

LSMA and ANN were applied to both the ASTER and ETM+ images. Impervious surface fraction image was extracted from each image. For the ASTER image, the RMSE of the result using the ANN model was 12.3%, and the one that resulted from LSMA was 13.2%. For the ETM+ image, the RMSE of the result from ANN was 16.7%, and the one from LSMA was 18.9%. Fig. 7 shows the scatter plots of the accuracy assessment results. These results indicate that, with both images, ANN performed better than LSMA. As a nonlinear model, the ANN model accounted better the energy interactions in the environment. The reflected energy was very complicated, and nonlinear spectral mixing prevailed. The LSMA model was based on an assumption that the spectrum of a pixel was a linear combination of the spectra of endmembers, which was not true in reality. The LSMA, as a simplified model, could still be an appropriate technique to estimate impervious surfaces, if we considered that the RMSE was just 1%–2% lower than the one that resulted from the ANN model. In contrast, ANN simulated how human brains processed spatial data and used nonlinear sigmoidal function to convert the inputs into desired outputs. The BP learning algorithm adjusted the weight for each artificial neuron to make sure that the outputs were close to a predefined accuracy level.

Although there were technical difficulties associated with ANN model, such as the hidden layers, learning rates, momentum factor, computing time, etc., in general, the ANN model
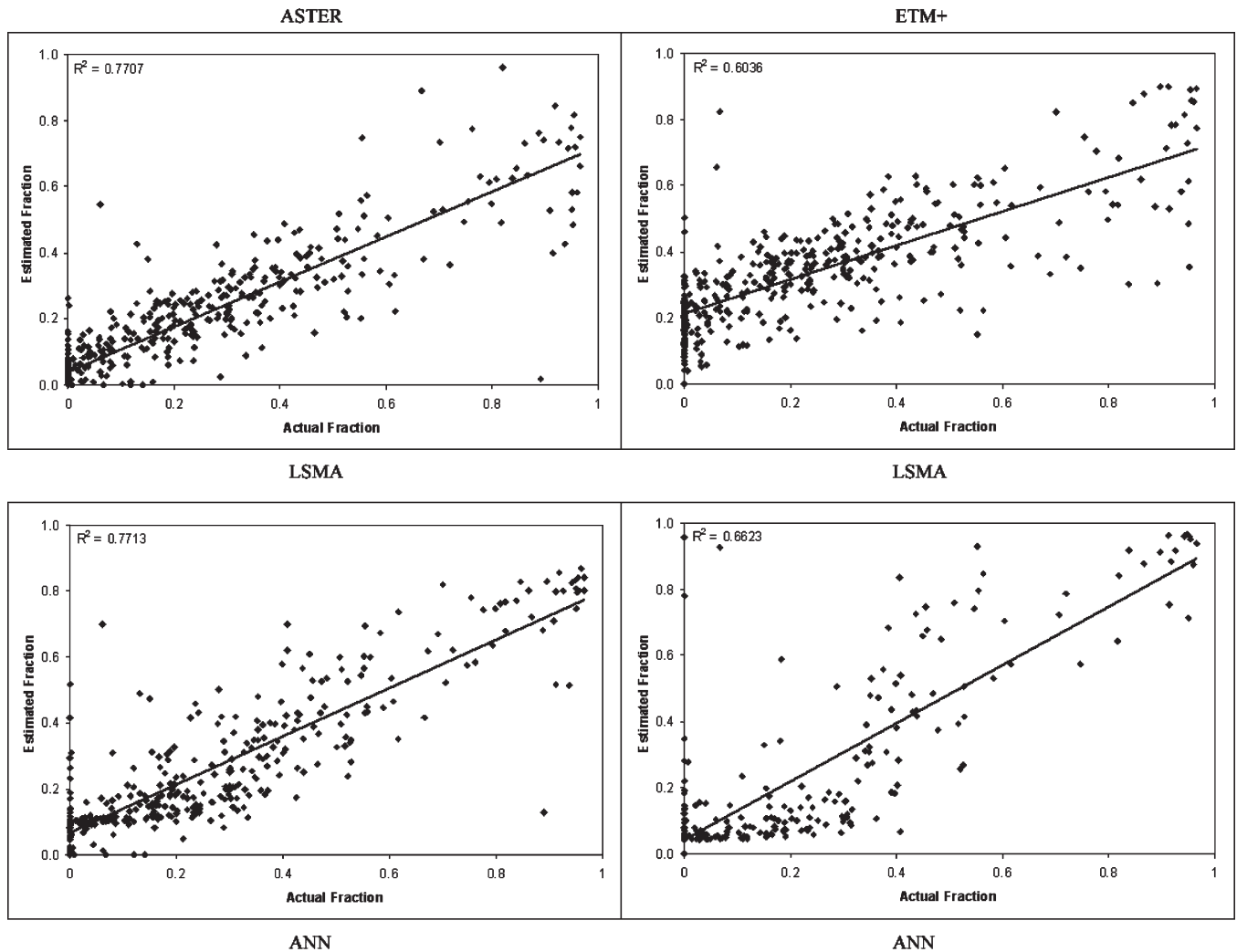
Fig. 7.   Scatter plots of the accuracy assessment results.

appeared more appropriate to estimate subpixel impervious surfaces from medium-resolution images. This conclusion suggests that ANN had a better capability to handle mixed pixels than LSMA.

In order to test the seasonal sensitivity of satellite images for estimating impervious surfaces, LSMA was conducted with two additional ASTER images of the same area, which were acquired on April 5, 2004, and October 3, 2000, respectively. The results were then compared in terms of RMSE. The June image had the highest accuracy, whereas the October image was better than the one in April. The October image possessed an RMSE of 19.8%, whereas the April image yielded an RMSE of 21.1%. This comparison indicates that the season effect had a fundamental impact on impervious surface estimation. The image acquired in the summer time was more appropriate for impervious surface estimation. Those acquired in the spring and fall tended to produce less accurate results. Our fieldwork in the study area suggests that the seasonal effect was due largely to plant phenology, specifically the changes that occurred in forestland, grassland, cropland, and pasture. Although there were other types of land use and land cover, changes took place in the study area, for example, the expansion of urban and built-up uses; these three images were acquired within three and

a half years. Our fieldwork showed that urbanization-related changes had little impact on the accuracy assessment of impervious surface maps. To a large extent, mapping impervious surfaces was the reverse of mapping vegetation abundance. This is because vegetation had a very different spectral signature from impervious surfaces. Thus, it was easy to differentiate them. When tree leaves fell off, remote sensors tended to sense the energy from tree trunks and twigs. Moreover, when crops were harvested, the bare soil is exposed. The spectral signature of dry soils was similar to that of bright impervious surfaces. This confusion would lead to a less accurate estimation of impervious surfaces inevitably. This is why the June image achieved a better result than the ones in April and October. In Indiana, in June 16, the grass had already grown up, the tree canopies had been fully developed, and the crops had started to grow. The vegetation abundance was very high at this time, probably among the highest during the year. Nevertheless, in April 5, the tree canopy had not appeared yet. The grass and pasture were in their very early stage, while there was no crop. The soils in the fields were sometimes mixed with crop stems, and at other times, they were exposed. In October 3, although the grass and the tree canopies began to degrade, most of them were still there with good conditions. The crops had

been harvested or turned into yellow. In the October image, croplands were clearly identifiable due to the change in their spectral signatures. The vegetation abundance in October was in between April and June. The change of vegetation abundance and the associated changes in its spectral signature had an obvious impact on image analysis in general and in impervious surface estimation and mapping in particular.

V. DISCUSSIONS

Because of its effectiveness in handling the mixed-pixel problem, LSMA, as a subpixel classifier, is gaining great interest in the remote sensing community in recent years. As a physically based image-analysis procedure, it supports repeatable and accurate extraction of quantitative subpixel information [24]. The different methods of impervious surface extraction based on the LSMA model have been developed. For example, impervious surface may be extracted as one of the endmembers in the standard SMA model [30]. Impervious surface estimation can also be done by the addition of high- and low-albedo fraction images, with both as the SMA endmembers [3]. Moreover, a multiple-endmember SMA method has been developed [31], in which several impervious surface endmembers can be extracted and combined. However, these SMA-based methods have a common problem, i.e., the impervious surface tends to be overestimated in the areas with small amount of impervious surface, but it is underestimated in the areas with large amount of impervious surface [5]. The low statistical accuracy of impervious surface maps is due largely to the linear assumption of SMA and the method of endmember selection.

To avoid these limitations in LSMA, ANN was introduced as a subpixel classifier to see if it can improve the accuracy of impervious surface estimation because ANN is not limited by linear assumption, and there is no need to select endmembers from the feature space. Our results indicate that the ANN model improved the statistical accuracy of impervious surface estimation, whether ASTER or Landsat ETM+ image was used. It is noted that, with our method, the selection of training samples was an important step, which related directly to the accuracy of the final result. Too many samples could lead to overfit to the data, whereas too few samples were not sufficient to have a good model. Samples should contain all the spectral variations within each cover class, and they need to be distributed evenly all over the image scene. Second, the number of hidden layers and the number of hidden-layer nodes were also significant. Although a lot of methods have been developed to determine the number of the hidden-layer nodes, it is impacted by many factors, including the number of input and output nodes and the training samples. As a result, some trials and errors need to be made to find the appropriate number of hidden-layer nodes. Another issue with ANN is how to set up the parameters properly. There are some parameters that need to be set up by the analyst, for example, learning rate, momentum factor, etc. Although there exist some heuristics in the literature for designing and implementing the ANN, these settings were not straightforward. For example, too large a learning rate could make the model unstable, whereas too small a learning rate could only find the local minimum and miss the

global minimum of function error. The image analysts had to try different combinations of parameters in order to get the best results.

VI. CONCLUSION

In this paper, both LSMA and ANN were conducted to extract impervious surfaces from an ASTER image and an ETM+ image of Indianapolis, IN, USA, which were acquired close to the anniversary date in June. An accuracy assessment was performed against a high-resolution digital orthophotograph, which is based on 400 samples of 90 by 90 m. The results show that both LSMA and ANN yielded reasonably good estimation accuracy. With either image, ANN performed a little better than LSMA. For the ASTER image, the error was 12.3% with ANN and 13.2% with LSMA, whereas for the ETM+ image, the error was 16.7% with ANN and 18.9% with LSMA. It is suggested that ANN had better capability in handling the mixed-pixel problem, which prevailed in the medium-resolution images of the urban areas. The nonlinear mixing of image spectrum and no need for endmember selection from a feature space provided advantages to the ANN model for subpixel estimation of impervious surfaces. However, whether this conclusion can be applied to other images of medium resolution, such as ALI images from EO-1, warrants a future study.

The seasonal effect on impervious surface estimation was further analyzed with LSMA by comparing the ASTER image acquired in June with two additional ASTER images acquired in different seasons. Results show that the seasonal effect had a fundamental impact on impervious surface estimation. The June image was more effective for impervious surface estimation than the one in October, which was, in turn, better than the April image. The principle of LSMA is the variance partitioning by PC transformation of multispectral imagery and mixing-space characterization [32]. The June image was most appropriate because there was full growth of vegetation, and the mapping of impervious surfaces was more effective with contrasting spectral response from green vegetation. The mixing space, which is based on the four endmembers, was perfectly 3-D. In contrast, there was significant amount of bare soils and grounds and nonphotosynthesis vegetation in the April image and, to a less extent, in the October image. Plant phenology caused changes in the variance partitioning and impacted the mixing-space characterization. These changes had a negative impact on the estimation of impervious surfaces.

REFERENCES

[1] C. L. Arnold, Jr. and C. J. Gibbons, "Impervious surface coverage: The emergence of a key environmental indicator," *J. Amer. Plan. Assoc.*, vol. 62, no. 2, pp. 243–258, 1996.

[2] E. Brabec, S. Schulte, and P. L. Richards, "Impervious surfaces and water quality: A review of current literature and its implications for watershed planning," *J. Plan. Lit.*, vol. 16, no. 4, pp. 499–514, 2002.

[3] C. Wu and A. T. Murray, "Estimating impervious surface distribution by spectral mixture analysis," *Remote Sens. Environ.*, vol. 84, no. 4, pp. 493–505, Apr. 2003.

[4] L. Yang, C. Huang, C. G. Homer, B. K. Wylie, and M. J. Coan, "An approach for mapping large-area impervious surfaces: Synergistic use of Landsat-7 ETM+ and high spatial resolution imagery," *Can. J. Remote Sens.*, vol. 29, no. 2, pp. 230–240, 2003.

[5] D. Lu and Q. Weng, "Use of impervious surface in urban land-use classification," *Remote Sens. Environ.*, vol. 102, no. 1/2, pp. 146–160, May 2006.

[6] D. Lu and Q. Weng, "Spectral mixture analysis of ASTER imagery for examining the relationship between thermal features and biophysical descriptors in Indianapolis, Indiana," *Remote Sens. Environ.*, vol. 104, no. 2, pp. 157–167, Sep. 2006b.

[7] Q. Weng, X. Hu, and D. Lu, "Extracting impervious surface from medium spatial resolution multispectral and hyperspectral imagery: A comparison," *Int. J. Remote Sens.* to be published.

[8] P. Fisher, "The pixel: A snare and a delusion," *Int. J. Remote Sens.*, vol. 18, no. 3, pp. 679–685, Feb. 1997.

[9] A. P. Cracknell, "Synergy in remote sensing—What's in a pixel?" *Int. J. Remote Sens.*, vol. 19, no. 11, pp. 2025–2047, Jul. 1998.

[10] M. Linderman, J. Liu, J. Qi, L. An, Z. Ouyang, J. Yang, and Y. Tan, "Using artificial neural networks to map the spatial distribution of understorey bamboo from remote sensing data," *Int. J. Remote Sens.*, vol. 25, no. 9, pp. 1685–1700, 2004.

[11] T. W. Ray and B. C. Murray, "Nonlinear spectral mixing in desert vegetation," *Remote Sens. Environ.*, vol. 55, no. 1, pp. 59–64, Jan. 1996.

[12] G. M. Foody, R. M. Lucas, P. J. Curran, and M. Honzak, "Nonlinear mixture modelling without end-members using an artificial neural network," *Int. J. Remote Sens.*, vol. 18, no. 4, pp. 937–953, Mar. 1997.

[13] P. M. Atkinson and A. R. L. Tatnall, "Introduction neural networks in remote sensing," *Int. J. Remote Sens.*, vol. 18, no. 4, pp. 699–709, Mar. 1997.

[14] D. L. Civco, "Artificial neural networks for land-cover classification and mapping," *Int. J. Geogr. Inf. Syst.*, vol. 7, no. 2, pp. 173–186, 1993.

[15] K. S. Chen, Y. C. Tzeng, C. F. Chen, and W. L. Kao, "Land-cover classification of multispectral imagery using a dynamic learning neural network," *Photogramm. Eng. Remote Sens.*, vol. 61, no. 4, pp. 403–408, 1995.

[16] G. M. Foody, M. B. McCulloch, and W. B. Yates, "Classification of remotely sensed data by an artificial neural network: Issues related to training data characteristics," *Photogramm. Eng. Remote Sens.*, vol. 61, no. 4, pp. 391–401, 1995.

[17] Y. Zhang, J. Gao, and J. Wang, "Detailed mapping of a salt farm from Landsat TM imagery using neural network and maximum likelihood classifiers: A comparison," *Int. J. Remote Sens.*, vol. 28, no. 10, pp. 2077–2089, 2007.

[18] M. Flanagan and D. L. Civico, "Subpixel impervious surface mapping," in *Proc. Amer. Soc. Photogramm. Remote Sens. Annu. Conv.*, St. Louis, MO, 2001. (unpaginated).

[19] S. Lee and R. G. Lathrop, "Subpixel analysis of Landsat ETM+ using self-organizing map (SOM) neural networks for urban land cover characterization," *IEEE Trans. Geosci. Remote Sens.*, vol. 44, no. 6, pp. 1642–1654, Jun. 2006.

[20] R. P. Mohapatra and C. Wu, "Subpixel imperviousness estimation with IKONOS imagery: An artificial neural network approach," in *Remote Sensing of Impervious Surfaces*, Q. Weng, Ed. Boca Raton, FL: CRC Press, 2007, pp. 21–37.

[21] W. Liu and E. Y. Wu, "Comparison of non-linear mixture models: Subpixel classification," *Remote Sens. Environ.*, vol. 94, no. 2, pp. 145–154, 2005.

[22] M. Pal and P. M. Mather, "An assessment of the effectiveness of decision tree methods for land cover classification," *Remote Sens. Environ.*, vol. 86, no. 4, pp. 554–565, Aug. 2003.

[23] J. B. Adams, D. E. Sabol, V. Kapos, R. A. Filho, D. A. Roberts, M. O. Smith, and A. R. Gillespie, "Classification of multispectral images based on fractions of endmembers: Application to land cover change in the Brazilian Amazon," *Remote Sens. Environ.*, vol. 52, no. 2, pp. 137–154, 1995.

[24] D. A. Roberts, G. T. Batista, J. L. G. Pereira, E. K. Waller, and B. W. Nelson, "Change identification using multitemporal spectral mixture analysis: Applications in eastern Amazônia," in *Remote Sensing Change Detection: Environmental Monitoring Methods and Applications*, R. S. Lunetta and C. D. Elvidge, Eds. Ann Arbor, MI: Ann Arbor Press, 1998, pp. 137–161.

[25] J. Lee, R. C. Weger, S. K. Senguta, and R. M. Welch, "A neural network approach to cloud classification," *IEEE Trans. Geosci. Remote Sens.*, vol. 28, no. 5, pp. 846–855, Sep. 1990.

[26] A. A. Green, M. Berman, P. Switzer, and M. D. Craig, "A transformation for ordering multispectral data in terms of image quality with implications for noise removal," *IEEE Trans. Geosci. Remote Sens.*, vol. 26, no. 1, pp. 65–74, Jan. 1988.

[27] T. Kavzoglu and P. M. Mather, "The use of backpropagating artificial neural networks in land cover classification," *Int. J. Remote Sens.*, vol. 24, no. 23, pp. 4907–4938, 2003.

[28] G. D. Garson, *Neural Networks: An Introductory Guide for Social Scientists*. London, U.K.: Sage, 1998.

[29] J. R. Eastman, *IDRISI Kilimanjaro: Guide to GIS and Image Processing*. Worcester, MA: Clark Univ. Press, 2003. (Manual Version 14).

[30] S. Phinn, M. Stanford, P. Scarth, A. T. Murray, and P. T. Shyy, "Monitoring the composition of urban environments based on the vegetation-impervious surface-soil (VIS) model by subpixel analysis techniques," *Int. J. Remote Sens.*, vol. 23, no. 20, pp. 4131–4153, Oct. 2002.

[31] T. Rashed, J. R. Weeks, D. A. Roberts, J. Rogan, and R. Powell, "Measuring the physical composition of urban morphology using multiple endmember spectral mixture models," *Photogramm. Eng. Remote Sens.*, vol. 69, no. 9, pp. 1011–1020, 2003.

[32] C. Small, "A global analysis of urban reflectance," *Int. J. Remote Sens.*, vol. 26, no. 4, pp. 661–681, 2005.

Qihao Weng (M'07) was born in Fuzhou, China, in 1964. He received the A.S. degree in geography from Minjiang University, Fuzhou, in 1984, the M.S. degree in physical geography from South China Normal University, Guangzhou, China, in 1990, the M.A. degree in geography from the University of Arizona, Tucson, in 1996, and the Ph.D. degree in geography from the University of Georgia, Athens, in 1999.

He is currently an Associate Professor of geography with the Department of Geography, Geology, and Anthropology, Indiana State University, Terre Haute, where he is the Director of the Center for Urban and Environmental Change. He is the author of more than 85 peer-reviewed journal articles and other publications, and the Series Editor for *Taylor and Francis Series in Remote Sensing Applications*. He has published the books *Urban Remote Sensing* (CRC Press, 2006) and *Remote Sensing of Impervious Surfaces* (CRC Press, 2007). His research focuses on remote sensing and geographic information system analysis of urban ecological and environmental systems, land-use and land cover changes, urbanization impacts, and human–environment interactions.

Dr. Weng is a member of the American Society of Photogrammetry and Remote Sensing (ASPRS), American Geophysical Union, and Association of American Geographers. He serves as the National Director of ASPRS (2007–2010) and the Secretary of the International Society for Photogrammetry and Remote Sensing Working Group VIII/1 (Human Settlement and Impact Analysis). He was the recipient of the Robert E. Altenhofen Memorial Scholarship Award by the ASPRS (1999) and the Best Student-Authored Paper Award from the International Geographic Information Foundation (1998). In 2006, he received the Theodore Dreiser Distinguished Research Award by Indiana State University, the university's highest research honor bestowed to faculty.

Xuefei Hu received the B.S. and M.S. degrees from the China University of Geosciences, Beijing. He is currently working toward the Ph.D. degree in the Department of Geography, Geology, and Anthropology, Indiana State University, Terre Haute.

He is also with the Center for Urban and Environmental Change, Indiana State University. His research interests focus on the estimation of impervious surface from remote sensing imageries, the use of artificial neural networks, and geographic information systems.